

CHANDRA OBSERVATION OF THE TEV SOURCE HESS J1834–087

ZDENKA MISANOVIC¹, OLEG KARGALTSEV² AND GEORGE G. PAVLOV^{3,4}¹School of Physics, Monash University, Melbourne, 3800 VIC, Australia (Zdenka.Misanovic@monash.edu)²Dept. of Astronomy, University of Florida, Gainesville, FL 32611-2055 (oyk100@astro.ufl.edu)³Dept. of Astronomy and Astrophysics, The Pennsylvania State University,
525 Davey Lab., University Park, PA 16802 (pavlov@astro.psu.edu)⁴St. Petersburg State Polytechnical University, Polytechnicheskaya ul. 29, St. Petersburg 195251, Russia

ABSTRACT

Chandra ACIS observed the field of the extended TeV source HESS J1834–087 for 47 ks. A previous *XMM-Newton* EPIC observation of the same field revealed a point-like source (XMMU J183435.3–084443) and an offset region of faint extended emission. In the low-resolution, binned EPIC images the two appear to be connected. However, the high-resolution *Chandra* ACIS images do not support the alleged connection. Instead, in these images XMMU J183435.3–084443 is resolved into a point source, CXOU J183434.9–084443 ($L \simeq 2.5 \times 10^{33}$ ergs s^{−1}, for a distance of 4 kpc; photon index $\Gamma \simeq 1.1$), and a compact ($\lesssim 20''$) nebula with an isotropic morphology and a softer spectrum ($L \simeq 4.2 \times 10^{33}$ ergs s^{−1}, $\Gamma \simeq 2.7$). The nature of the nebula is uncertain. We discuss a dust scattering halo and a pulsar-wind nebula as possible interpretations. Based on our analysis of the X-ray data, we re-evaluate the previously suggested interpretations of HESS J1834–087 and discuss a possible connection to the *Fermi* LAT source 1FGL J1834.3–0842c. We also obtained an upper limit of 3×10^{-14} ergs cm^{−2} s^{−1} on the unabsorbed flux of the SGR J1833–0832 (in quiescence), which happened to be in the ACIS field of view.

Subject headings: gamma rays: individual (HESS J1834–087, 1FGL J1834.3–0842c)—stars: neutron—
supernova remnants: individual (W41=G23.3–0.3)—X-rays: individual (CXOU
J183434.9–084443, XMMU J183435.3–084443)

1. INTRODUCTION

Surveys of the Milky Way plane with modern Imaging Atmospheric Cherenkov Telescopes (IACTs) have revealed more than 70 sources of very high energy (VHE) γ -rays¹. While X-ray binaries (XRBs), young stellar clusters and background AGNs have all been proposed as possible sources of emission in the TeV energy range, the majority of the classified Galactic γ -ray sources are thought to be associated with pulsar wind nebulae (PWNe) and supernova remnants (SNRs) (Aharonian et al. 2005, 2006; Gallant et al. 2008; Kargaltsev & Pavlov 2010). However, about 30% of the cataloged VHE sources lack reliable classifications. Furthermore, for many classified sources there remains an uncertainty about the actual mechanism responsible for the production of the VHE γ -rays. Therefore, multiwavelength studies and modeling of the VHE source population are of a great interest at the present time.

The two main mechanisms for the production of high-energy γ -rays are the inverse Compton (IC) scattering of low-energy photons, and the hadronic collisions, in which the energetic protons colliding with ambient particles produce neutral pions, which decay into high-energy photons ($\pi^0 \rightarrow 2\gamma$; see, e.g., Hinton & Hofmann 2009). Rotation-powered pulsars emit highly energetic pulsar wind (PW), which is responsible for the synchrotron radiation observed from radio up to MeV energies (see Kargaltsev & Pavlov 2008, 2010, for recent reviews). It is believed that the γ -ray PWN can be produced when the ambient microwave, optical or infrared photons are upscattered by relativistic PW electrons up to the GeV and TeV energies. While the X-ray PWNe are powered

by energetic electrons injected/accelerated in the vicinity of the pulsar (Lorentz factor $\sim 10^8$), the VHE PWNe are powered by cooled, less-energetic electrons (Lorentz factor $\sim 10^7$), which have propagated further away from the pulsar (e.g., de Jager & Djannati-Ataï 2008). The IC cooling time of these γ -ray-producing electrons is longer than that of the electrons that produce X-rays, and hence, they trace the cumulative history of the PWN, similar to radio emission (the relic PWN model). If the pulsar contains a hadronic component, the VHE emission could also be produced via a hadronic process when relativistic PW hadrons encounter dense material such as the host SNR shell. An alternative possibility is that the SNR shock accelerates protons, which then interact with the dense ISM (e.g., a molecular cloud) and produce VHE emission.

The extended source HESS J1834–087 ($18.7 \pm 2.0 \times 10^{-12}$ photons cm^{−2} s^{−1} at $E > 200$ GeV, photon index $\Gamma = 2.5 \pm 0.2$; Aharonian et al. 2005, 2006) is spatially coincident with the center of the radio shell SNR G23.3–0.3 (W41; Kassim 1992), making the remnant a promising candidate for generating the observed γ -ray emission. However, the smaller size of the HESS source² (diameter $\sim 10'$ compared to the SNR diameter of $\sim 30'$) and the projected location well within the SNR shell suggest that the γ -ray emission does not come from the entire SNR shell as it has been seen in other SNRs firmly associated with HESS sources (e.g., Acero et al. 2009). Albert et al. (2006) detected the TeV source with the *Major Atmospheric Gamma Imaging Cerenkov (MAGIC)* telescope, confirmed its extension, and measured the flux consistent with the HESS measurement.

The region was also observed in radio with the Very

¹ See <http://tevcat.uchicago.edu/>² See Table 3 and Section 5.1 in Aharonian et al. (2006).

Large Array (VLA), as part of the Galactic Plane survey in continuum and in CO molecular line emission, and also in X-rays with *XMM-Newton*. Based on these observations, Tian et al. (2007) estimated the remnant's age ($10^4 - 10^5$ yrs) and the distance (4 kpc), and suggested that the observed γ -ray emission is produced by a hadronic process when the particles accelerated by the SNR shock interact with a giant molecular cloud (GMC) projected near the center of W41 (see also Yamazaki et al. 2006). Another explanation was put forward by Bartko & Bednarek (2008), who proposed the nearby pulsar J1833-0827 (=B1830-08; $24'$ away from the center of the HESS 1834-078) as the source of relativistic electrons. These electrons were ejected at the pulsar's birth place, presumably near the SNR center, i.e., within the extent of the HESS source (a relic PWN). Gaensler & Johnston (1995) argued that the association of the PSR J1833-0827 and W41 is plausible, given the pulsar's characteristic age of 148 kyr and the corresponding projected velocity of $\sim 250 \text{ km s}^{-1}$, required to move the pulsar from its birthplace to the current location. However, in a recent analysis of the *XMM-Newton* data, Schmitt et al. (2010, to be submitted to ApJ) rules out the association of B1830-08 and W41. Schmitt et al. detected a possible PWN surrounding the pulsar, but since the morphology of the nebular emission does not resemble a bow-shock, they concluded that the pulsar does not move fast enough to travel from the center of W41 to its current position, approximately $26'$ away.

Subsequent analysis of the *XMM-Newton* observations (Mukherjee et al. 2009, hereafter M+09) revealed a bright point-like source XMMU J183435.3-084443 at the center of W41 apparently connected to a region of faint extended emission also located within the extent of the HESS source. M+09 have argued that the new pulsar/PWN candidate is the most likely counterpart of HESS J1834-087.

To discriminate between these alternative scenarios, we have observed the region of the TeV source with the *Chandra* ACIS detector. In Section 2 we present the multiwavelength data on HESS J1834-087, which, in addition to the *Chandra* observation, also include archived radio, infrared (IR) and γ -ray data. We further discuss our results in Section 3 and summarize them in Section 4.

2. OBSERVATIONS AND RESULTS

We observed the region around HESS J1834-087 on 2009 June 7 with *Chandra* ACIS (ObsID 10126) for 47.5 ks (46.5 useful scientific exposure) in timed exposure (TE) mode using very faint (VF) telemetry format. The point source was imaged on the S3 chip approximately $15''$ away from the nominal aimpoint, placing a large part of the extended emission detected by *XMM-Newton* on the same chip. In addition, S1, S2, S4, I1 and I2 chips were also activated during the observation. We used CIAO 4.2 and CALDB 4.2.2 for our analysis. We have applied additional particle background cleaning for the VF mode, using the pulse heights in the outer 16 pixels of the 5×5 event island to help distinguish between “good” X-ray events and “bad” events that are most likely associated with cosmic rays. We also made extensive use of the archival multiwavelength data of this region obtained with *XMM-Newton*, VLA and *Spitzer* to compare them with the *Chandra* images.

2.1. Spatial analysis

2.1.1. Previous multiwavelength observations

Figure 1 shows the VLA 20-cm image of W41 (White et al. 2005), revealing fine details of the highly structured partial shell with a diameter of $\sim 30'$, and also some extended radio emission near the center. However, no point radio sources are visible, and no detection of radio pulsations from within the SNR shell has been reported so far. The extended VHE source HESS J1834-087 is located near the SNR center. With an angular extent of $5.4'$ in radius (see Table 3 in Aharonian et al. 2006) the TeV source appears to be significantly smaller than the SNR shell (Figure 1, left).

The middle panel of Figure 1 shows the innermost region of the extended TeV source as it is seen in a 17 ks exposure by *XMM-Newton* EPIC (for the analysis of *XMM-Newton* data see Tian et al. 2007, M+09). M+09 detected a total of 16 point-like sources in the FoV of the MOS detectors, with one of the brightest sources well within the extent of the TeV emission. Furthermore, in the EPIC images this bright point-like source (XMMU J183435.3-084443) appears to be accompanied by extended X-ray emission, also located within the extended TeV source. The spectral analysis of the *XMM-Newton* data indicates that both the point-like source and diffuse emission (designated XMMU J183435.3-084443 and G23.234-0.317, respectively; M+09) are highly absorbed and most probably non-thermal, although the spectral parameters for the diffuse emission are not well constrained due to the large background contribution. GLIMPSE³ $8\mu\text{m}$ image (Figure 1, bottom) shows no correlation between the diffuse X-ray and IR emission.

2.1.2. Images

Our *Chandra* observation resolved XMMU J183435.3-084443 into a point source, which we designate CXOU 183434.9-084443 (centered at R.A.= $18^{\text{h}} 34^{\text{m}} 34^{\text{s}}.944$, Decl.= $-08^{\circ} 44' 43''.09$), and a compact diffuse emission extending up to $\simeq 20''$ from the point source (Figure 2, top), with more or less isotropic surface brightness distribution, and an average surface brightness of $0.8 \text{ cts arcsec}^{-2}$ in an annulus with radii $1''.5$ and $10''$ ($S/N \approx 14$). To separate the X-ray diffuse emission from the PSF wings of the pulsar candidate image, we have simulated a PSF, using MARX⁴ and assuming the measured spectral properties of CXOU J183434.9-084443. The comparison of the data and point source simulation (Figure 3) suggests a good agreement between the data and simulation in a small aperture (approximately up to $1''$ radius) while the extended emission is easily seen at larger radii. The 2MASS image of the same region (Figure 2, bottom) shows no near-infrared (NIR) sources within $6''$ from CXOU J183434.9-084443 position.

We searched for other point sources in the ACIS image in particular within the extent of the HESS source. We

³ The Galactic Legacy Infrared Mid-Plane Survey; see <http://www.astro.wisc.edu/sirtf>

⁴ For the MARX simulation we used the same off-axis and roll angles, and the detector parameters as in the real observation, but increased the exposure time by a factor of 100 (rescaling the resulting image) to reduce the statistical errors. We found that using the dither blur parameter of $0''.35$ gives the best match between the data and simulation.

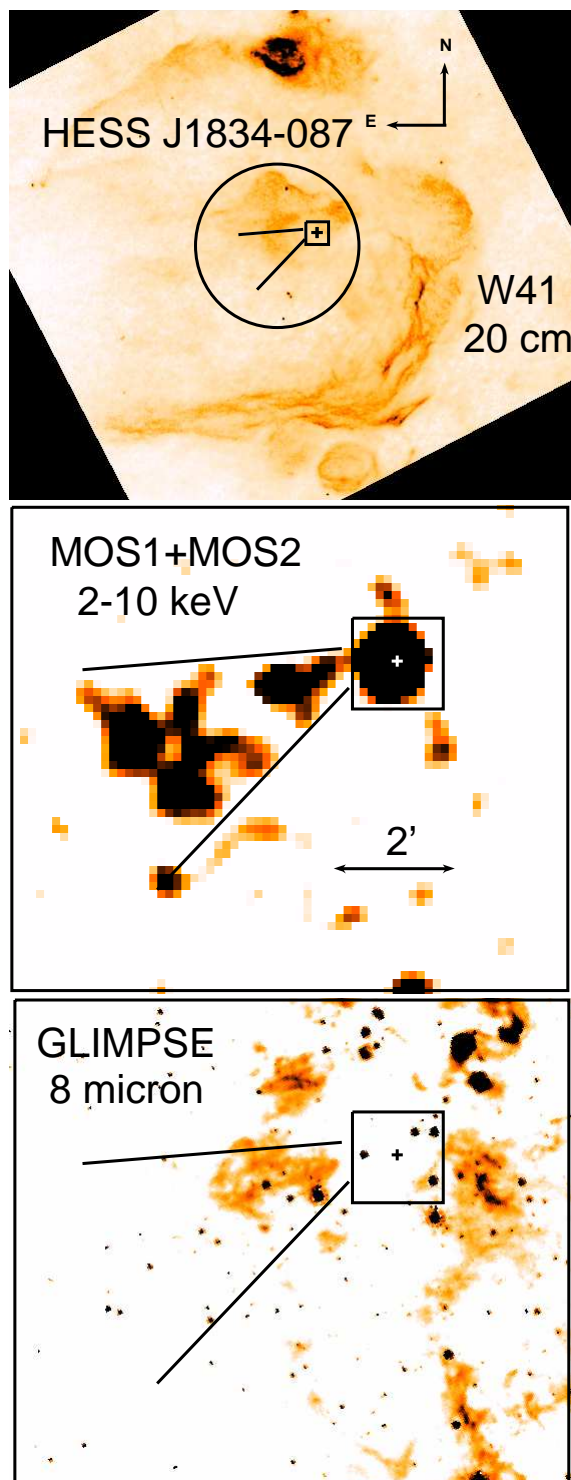


FIG. 1.— *Top*: VLA 20-cm image of the SNR G23.3-0.3 (W41) showing its highly structured partial shell with a diameter of $\sim 30'$ and some enhanced emission near the center (White et al. 2005). The circle (radius $5.4'$) shows the position and extent of HESS J1834-087 as measured by Aharonian et al. (2006). *Middle*: Broad-band (0.2–10 keV) *XMM-Newton* 17 ks image of the interior of W41 combining MOS1 and MOS2 data (see also M+09). The image with the pixel size of $8''$ is smoothed with a Gaussian of FWHM $40''$. The cross marks the position of CXOU 183434.9-084443 (see text). Higher-resolution images of the vicinity of CXOU 183434.9-084443 are shown in Figure 2. The tail-like emission detected in the *XMM-Newton* observation is marked in all panels. *Bottom*: GLIMPSE (8 micron) image of the same region of the sky as in the middle panel.

found a faint (~ 30 cts in 0.5–8 keV) point-like source at R.A. = $18^{\text{h}} 34^{\text{m}} 42^{\text{s}}.6$, Decl. = $-08^{\circ} 45' 01''95$, approximately $2'$ east of the pulsar candidate (Figure 4, top). The source coincides with the region of the enhanced “tail” emission detected by M+09, although no point source was detected at that position in the *XMM-Newton* data. This could be due to the lower angular resolution and higher EPIC background or due to the transient nature of the source. The *Chandra* spectrum of this source is soft, with an absorption column almost an order of magnitude lower than that of the candidate pulsar/PWN. Furthermore, the X-ray source coincides with a 2MASS source, suggesting that it is a foreground star. Most of the point-like X-ray sources detected in the *XMM-Newton* data (Table 1 of M+09) are either outside the FoV of the activated ACIS chips, far off-axis, or near the chip edges, but we did detect the bright sources 11 and 15 on I2 and I3 chips, respectively (following the source designation by M+09). The X-ray spectra of these sources are relatively soft, with absorption columns $N_{\text{H}} = (1-9) \times 10^{21} \text{ cm}^{-2}$, suggesting that they are relatively nearby. Source 15 coincides with a faint 2MASS source, already listed in Table 1 of M+09. Using our more accurate *Chandra* position, we also find two bright 2MASS sources within the *Chandra* error circle of the source 11. We also found that the position of the recently detected SGR J1833-0832 (Gelbord et al. 2010; Göğüş et al. 2010) is within the ACIS FoV, near the edge of the S1 chip (Figure 4, bottom), but we did not detect any source at this position. After correcting for the vignetting, and assuming the spectral parameters reported by Gelbord & Vetere (2010), we obtained an upper limit of $3 \times 10^{-14} \text{ ergs cm}^{-2} \text{ s}^{-1}$ on the unabsorbed flux of the SGR in quiescence.

While looking for high-energy sources within the ACIS FoV, we found *Fermi* LAT source 1FGL J1834.3-0842c (0.11 Crab in 1–100 GeV, photon index $\Gamma = 2.24 \pm 0.04$; Abdo et al. 2010) located $\sim 5'$ northwest of CXOU 183434.9-084443. The 95% error ellipse of the 1FGL J1834.3-0842c position also includes the north-western part of the SNR shell (Figure 4, bottom). The only X-ray source detected within the error ellipse of the *Fermi* LAT source is a relatively faint source, CXOU 183430.3-084142.8, with a bright optical counterpart, located at the edge of the GeV emission. This source is apparently a foreground star, most likely not associated with the GeV emission.

Figure 4 (top) shows the large-scale ACIS image, which covers the region of the extended HESS source. The heavily smoothed image shows some faint extended emission, which must be a part of the large-scale emission seen in the *XMM-Newton* images. Indeed, a closer comparison of the two images (see Figure 1) shows that the extended emission visible in the ACIS image coincides with the brightest regions seen in the *XMM-Newton* data. However, the origin of this emission remains elusive. We see no clear connection between CXOU 183434.9-084443 and the extended emission $3' - 4'$ east-southeast of it. Its association with the SNR is also questionable, as it does not seem to coincide spatially with the radio shell or with the diffuse radio emission in the SNR interior (Figure 4, middle and bottom). To investigate the nature of this extended emission, its spectrum must be measured in a

long observation.

XMMU J183435.3–084443 has also been detected by the *Swift* (Landi et al. 2006). M+09 included the three archived *Swift* observations in their analysis, but could not make any firm conclusions about intrinsic flux variability of XMMU J183435.3–084443 (the count rate measured in the third observation showed a 3σ increase over the first two, or 2σ increase over the mean rate). To search for variability in the ACIS observations, we produced light-curves with a bin size ranging from $\sim 10^2$ to 10^3 seconds, but could not see any significant flux variations on the time-scales relevant for the ACIS data (i.e., considering the length and time resolution of the ACIS observation). Our *Chandra* data allowed us to search for pulsations in the 6–100 s period range, but we did not find any periodic signal.

2.2. Spectral analysis

To minimize the contribution from the nebula, we extracted the X-ray spectrum of CXOU J183434.9–084443 from a circular region with a radius of $1''$ centered on the point source (see Figure 3), while the background photons were extracted from an annulus with the inner and outer radii of $1''.5$ and $5''.5$, respectively. A total of 220 counts were detected in the $r = 1''$ aperture in the 0.5–8 keV band. The comparison with the simulated point source suggests that approximately 30 of these counts are from the nebula, while the contribution from the background is negligible (1–2 counts), implying an aperture-corrected⁵ count rate of 4.80 ± 0.04 cts ks⁻¹. For spectral fitting these counts were grouped to a minimum of 15 counts per bin.

To measure the nebular spectrum, we extracted a total of 208 photons from the $1''.5$ – $10''$ annulus centered on CXOU J183434.9–084443, while the background contribution was measured from an annulus with $10'' < r < 20''$. We estimate that there are ~ 50 counts from the true background and ~ 10 counts from the PSF wings in the same aperture, implying a count rate of 3.2 ± 1.1 cts ks⁻¹ for the background- and PSF-subtracted emission. The nebula spectrum was also grouped to a minimum of 15 counts per bin.

The small number of counts and the lack of soft emission (the spectra are virtually cut off below 3 keV; see Figure 5) did not allow us to constrain well the spectral model parameters. We fit the spectra with absorbed power-law (PL) models and show the results in Table 1 and Figures 5 and 6. We first fit each spectrum independently and noticed that the absorption columns for the point source and for the diffuse emission region were similar ($2.8^{+2.8}_{-1.3}$ and $2.8^{+2.9}_{-1.5} \times 10^{23}$ cm⁻², respectively), suggesting a common distance. To determine the value of the absorption column more accurately, we then performed a simultaneous fit with the MOS1 and MOS2 spectra⁶ of XMMU J183435.3–084443, assuming again a common absorption column density (i.e., linking this

parameter when fitting the spectra simultaneously, with other parameters untied).

After obtaining the best-fit value for N_H , we fixed this parameter before fitting the ACIS spectra of the point source and the nebula individually and calculating the errors for other model parameters and for the fluxes (Table 1). The unabsorbed luminosities are calculated for the 0.5–8 keV band assuming a distance of 4 kpc (Tian et al. 2007). We note that the large absorption measured from the X-ray spectra is more than an order of magnitude higher than the estimated N_{HI} value for the Galaxy in that direction ($\sim 2 \times 10^{22}$ cm⁻²; Dickey & Lockman 1990), implying a large amount of molecular material in the line of sight (see Tian et al. 2007, and references therein).

⁵ From the radial profile of the simulated PSF and the data (Figure 3) we estimated the point source contribution of 85% in this aperture.

⁶ The MOS spectra were only used to measure the absorption column, because they contain not only photons from the pulsar candidate but also a large fraction of the compact nebula that could not be resolved.

TABLE 1
ABSORBED PL MODEL FITS TO THE SPECTRA OF CXOU J183434.9-084443 AND SURROUNDING EXTENDED EMISSION.

	N_{H} 10^{23} cm^{-2}	Γ	PL Norm. $10^{-4} \text{ cm}^{-2} \text{ s}^{-1} \text{ keV}^{-1}$	$\chi^2_{\nu}/\text{d.o.f}$	Absorbed Flux $10^{-13} \text{ ergs cm}^{-2} \text{ s}^{-1}$	Luminosity $10^{33} \text{ ergs s}^{-1}$
Point source	2.72 (frozen)	$1.09^{+0.40}_{-0.42}$	$0.95^{+0.92}_{-0.47}$	0.81/13	$2.56^{+0.22}_{-0.22}$	$2.3^{+0.6}_{-0.4}$
Nebula	2.72 (frozen)	$2.73^{+0.54}_{-0.53}$	$6.8^{+9.1}_{-3.9}$	0.64/13	$0.98^{+0.13}_{-0.12}$	$4.1^{+4.8}_{-1.9}$

NOTE. — The absorption column density was frozen at its best-fit value determined in the joint fit with XMM-Newton data (MOS1 and MOS2 spectra of the point-like source XMMU J183435.3-084443). The observed flux and unabsorbed luminosity, $L_X = 4\pi d^2 F_X^{\text{unabs}}$, are calculated for the 3–8 keV and 0.5–8 keV energy band, respectively, for the distance $d = 4$ kpc. The listed uncertainties are at a 1σ confidence level. The observed flux and unabsorbed luminosity of CXOU J183434.9-084443 are aperture-corrected.

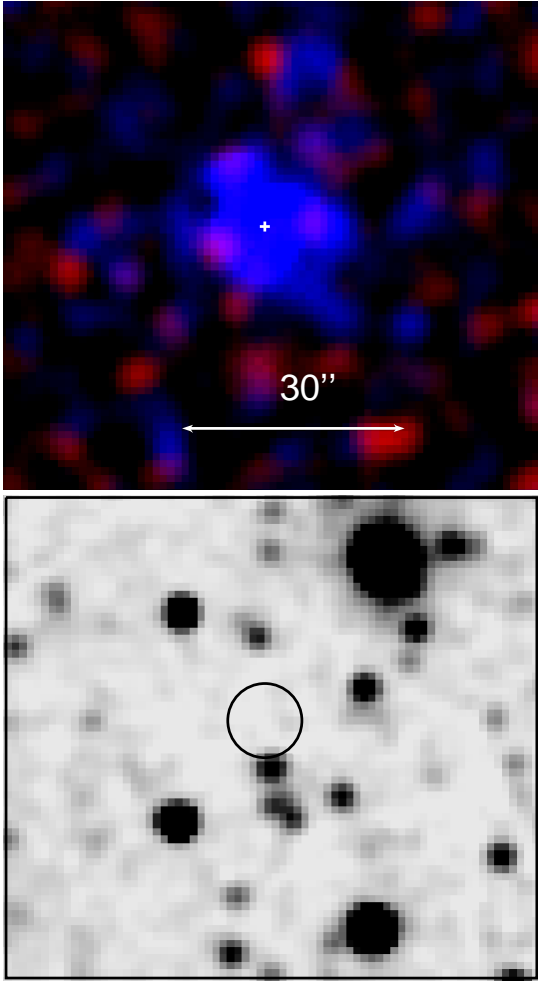


FIG. 2.— *Top*: Chandra ACIS $90'' \times 90''$ two-color (red: 0.5–2 keV; blue: 2–8 keV) image of the region around the pulsar and compact PWN candidate coinciding with HESS 1834-078. The image is binned to a pixel size of $1''$ and smoothed with a Gaussian of FWHM $\sim 4''$. *Bottom*: 2MASS image of the same region. The position of the pulsar candidate is marked by a circle with a radius of $5''$.

3. DISCUSSION

Chandra resolved the compact extended emission surrounding CXOU J183434.9-084443, which is by far the brightest X-ray source located within the extent of HESS J1834-087. It was previously suggested that the

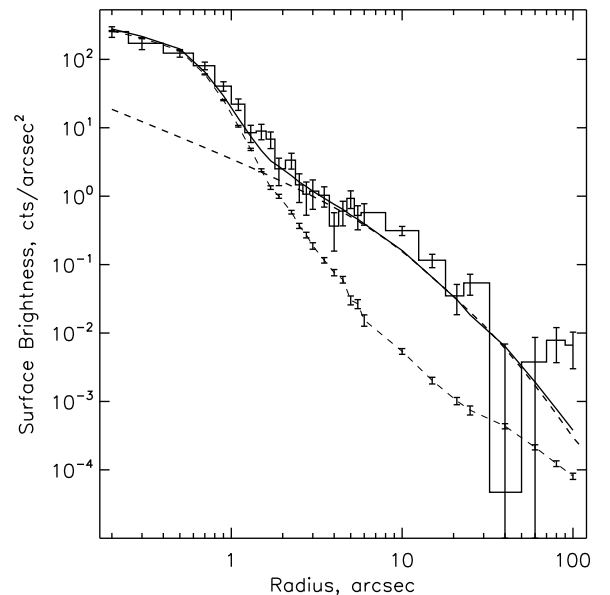


FIG. 3.— The radial profiles (in 3–8 keV) of the simulation and data showing the contribution of the extended emission in the vicinity of the point source. The dashed line with errorbars shows the PSF profile of the point source simulated using MARX (see text). The histogram shows the radial distribution of the surface brightness measured in annular regions centered on the point source. The background level of $0.15 \text{ cts arcsec}^{-2}$ has been subtracted from the data. The dashed line without errorbars shows possible contribution of a dust halo (see Section 3.1.1 and Appendix, equations A6 and A7).

TeV emission could arise either as a result of interaction between the SNR shock and the GMC near W41 (Tian et al. 2007), or alternatively, it could be due to a PWN powered by CXOU J183434.9-084443 (M+09). Below we discuss the constraints that our observation places on the nature of CXOU J183434.9-084443 and HESS J1834-087. We also explore a possible link between these sources and the recently discovered *Fermi* LAT source 1FGL J1834.3-0842c which is also located within SNR W41.

3.1. CXOU J183434.9-084443 and its extended emission

The point source appears to have a strongly absorbed spectrum that fits hard PL. The flux, PL slope, and

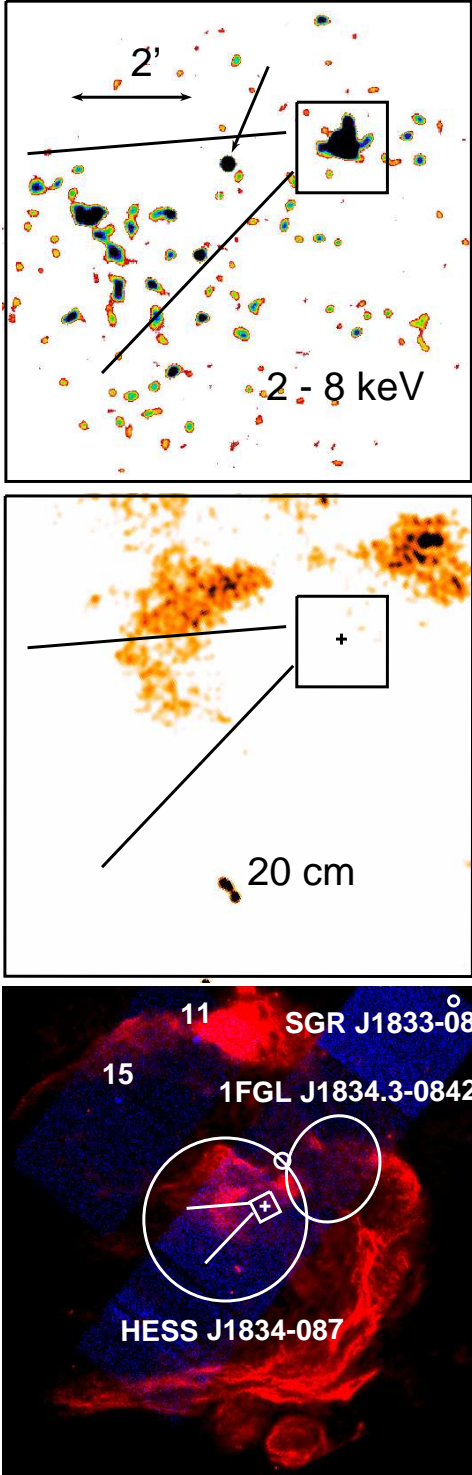


FIG. 4.— *Top*: Large-scale, smoothed with a Gaussian of FWHM $\sim 10''$, *Chandra* ACIS image (2–8 keV) encompassing the region of the extended tail-like emission detected with *XMM-Newton* (see Figure 1). The arrow shows the point source with a bright 2MASS counterpart (see text). *Middle*: VLA image of the same region. The enhanced extended radio emission in the center of W41 does not seem to coincide with the diffuse X-ray emission. *Bottom*: A two-color image (red: 20 cm; blue: 0.5–8 keV) showing the whole W41 and also the projected ACIS chips activated in the *Chandra* observation. The extent of the TeV source is marked by the big circle (radius $5.4'$) while the GeV source is shown by its 95% positional error ellipse ($6.0 \times 7.2'$). Several X-ray sources detected in the FoV are marked, including the star candidate at the edge of the GeV emission (small circle), and sources 11 and 15 as numbered in Table 1 by M+09. The position of the SGR J1833-0832 is also marked with a small circle.

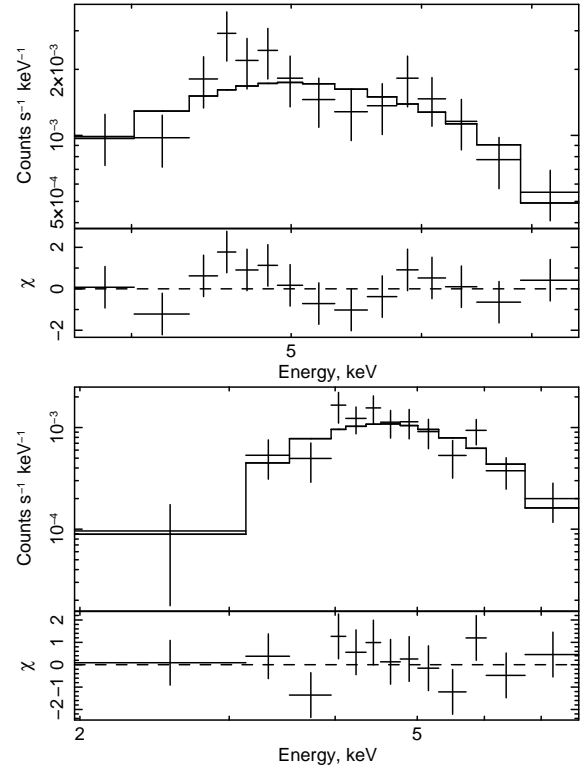


FIG. 5.— *Top*: The X-ray spectrum of the pulsar candidate extracted from the *Chandra* observation, and the corresponding best-fit absorbed PL model. The absorption column is frozen to its best fit-value (see Table 1) determined from the fit combining the *Chandra* and *XMM-Newton* data (see text). *Bottom*: The X-ray spectrum of the PWN candidate extracted from the *Chandra* data and the corresponding absorbed PL model, assuming the same absorption column as for the pulsar candidate (Table 1).

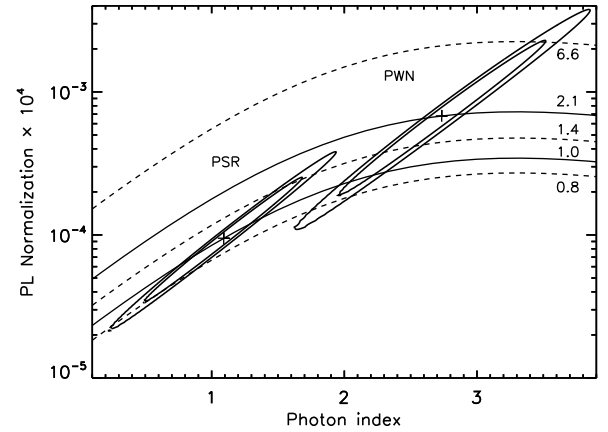


FIG. 6.— 90% and 99% confidence contours and the unabsorbed fluxes (0.5–8 keV) in units of 10^{-12} ergs cm^{-2} s^{-1} for the pulsar and PWN candidate.

the lack or any counterparts at lower frequencies make CXOU J183434.9–084443 a plausible candidate for a young remote pulsar. However, other options, such as an AGN seen through the Galactic plane, or a quiescent, obscured XRB (similar to those discovered with *INTEGRAL*), remain viable. Although the latter interpretation could explain the observed large N_H by the intrinsic absorption, we do not find any evidence of variability

or an iron line which are commonly seen in obscured HMXBs (Walter et al. 2006). It seems rather plausible that a large amount of molecular material is generally present along this line of sight; for instance, Göğüş et al. (2010) found $N_{\text{H}} \simeq 10^{23} \text{ cm}^{-2}$ while fitting the spectrum of the nearby SGR 1833-0832 in the active state.

An important piece of evidence, which we will consider in detail, is a compact, $r \lesssim 20''$, extended emission, which has been clearly resolved from the point source (Figures 2 and 3). This emission appears to be approximately symmetric and exhibits a much softer spectrum compared to that of the point source ($\Gamma = 2.7 \pm 0.5$ vs. 1.1 ± 0.4). Two most likely interpretations are a PWN around a young pulsar in W41, or a dust scattering halo around the strongly absorbed point source. A combination of the two is also a possibility. In fact, a hint of a plateau (or non-monotonic behavior) seen in Figure 3 between $3''$ – $10''$ may indicate at two possible components with different dependence on r .

3.1.1. A dust halo around a point source?

The very large absorbing column measured in X-rays suggests a significant dust column that should lead to an extended dust scattering halo (e.g., Predehl & Schmitt 1995). The halo brightness grows with the increasing intervening dust column, which is usually assumed to be proportional to the hydrogen absorption column, N_{H} , measured from X-ray spectra. More specifically, the scattering optical depth $\tau_{\text{scat}} \simeq S(N_{\text{H}}/10^{22} \text{ cm}^{-2})(E/1 \text{ keV})^{-2}$ for $S \simeq 0.5$ found by Predehl & Schmitt (1995) gives $\tau_{\text{scat}} < 1$ at $E > 3.7$ keV for CXOU J183434.9-084443, whose spectrum virtually cuts off below 3 keV (see Figure 5). Although taking into account multiple scatterings would be more accurate, the large uncertainties of the other parameters (such as the dust grain properties and dust distribution; see Appendix) do not warrant this extra complication. Therefore, we have used the single scattering approximation to calculate the halo profile by convolving the spectral intensity of a halo with the detector response in the 3–8 keV energy range. We find that for the parameters $\Theta = 360''$ and $S \simeq 1$, and for the dust distribution function $f(x)$ defined in the Appendix (equation A8), the dust halo model generally describes the observed radial profile (see Figure 3). However, some deviations are noticeable, hinting at a possibility of a second emission component. The dust distribution function $f(x)$, used in the calculation of the halo model shown in Figure 3, suggests that at least some dust must be located near the source, in agreement with the extreme absorption, which could be attributed to the local molecular clouds that are known to exist in this region of sky (Albert et al. 2006).

We should, however, point out that, in addition to the freedom of choosing the functional dependence of dust distribution with the distance, the approximate dust scattering model we use has two other free parameters (S and Θ), which can attain values within rather broad ranges, depending on the unknown properties of the dust grains along this particular line of sight (see Appendix). Therefore, the mere fact that the model qualitatively describes the observed radial profile does not guarantee that the extended emission is indeed a dust halo. On the other hand, the symmetric shape and the softer spectrum of the extended emission support at least partial

contribution of a dust halo. Although the dust halo interpretation of the extended emission does not rule out the young pulsar option for the point source, it allows for additional possibilities, such as a magnetar, an ANG, or an XRB.

3.1.2. A pulsar-wind nebula?

Let us now assume that CXOU J183434.9-084443 is a pulsar, and a substantial fraction of the observed extended emission around it is a PWN. The symmetric morphology of the candidate compact PWN would then suggest that the putative pulsar does not move very fast. Even if the pulsar was born at the geometrical center of the SNR (i.e., $\sim 2'$ from its current position) 100 kys ago, its transverse speed would only be $22d_4 \text{ km s}^{-1}$, which is in agreement with the nearly isotropic PWN shape. Thus, the large-scale emission east of the pulsar is not expected to be akin to long collimated tails formed behind supersonically moving pulsars, such as observed by Kargaltsev et al. (2008). Indeed, the high-resolution X-ray images of those tails show that the surface brightness is usually the highest near the pulsar, and it gradually decreases with the distance from the pulsar, i.e., the opposite of what we see in this case. It could be, however, that the large-scale X-ray emission is akin to that in the Vela X PWN, where the X-ray emission is offset from the pulsar and thought to come from the relic pulsar wind crushed and pushed aside by the reverse SNR shock (e.g., LaMassa et al. 2008).

The slope of the extended emission spectrum, fitted with the absorbed PL model, is rather steep, $\Gamma = 2.7 \pm 0.8$, albeit uncertain. For a PWN, such a steep slope is unusual because the X-ray spectra of most⁷ PWNe have $\Gamma = 1 - 2$ (e.g., see Figure 6 in Kargaltsev & Pavlov 2008). The steep slope may, however, be indicative of strong synchrotron cooling. The ratio of the extended and point source luminosities, $L_{\text{PWN}}/L_{\text{PSR}} \sim 1.8$, is typical of PWNe (see Figure 5 in Kargaltsev & Pavlov 2008). The spin-down power of the putative pulsar powering the PWN can be estimated as $\dot{E} = 4\pi r_s^2 c p_{\text{amb}}$, where r_s is the termination shock radius and p_{amb} is the ambient pressure. In the Sedov expansion phase, the pressure inside the SNR could be estimated from its radius by using a simple formula $p_{\text{amb}} = 3E/4\pi R^3$, where it is usually assumed that the total SNR explosion energy $E = 10^{51}$ ergs (e.g., see O’C. Drury et al. 2009). The estimated pressure $p_{\text{amb},-9} = p_{\text{amb}}/10^{-9} \text{ dyne cm}^{-2}$ and the termination shock radius scaled to a plausible value $r_{s,17} = r_s/10^{17} \text{ cm}$ (corresponding to $2.7''$ at the W41 distance of $d_4 = 4 \text{ kpc}$) give $\dot{E} = 4 \times 10^{36} r_{s,17}^2 p_{\text{amb},-9} \text{ erg s}^{-1}$ – a value typical for a young Vela-like pulsar. This estimate is sensitive to the value of $r_{s,17}$, which could be a factor of a few smaller than the scaling chosen⁸. The luminosity of the compact PWN, $\simeq 4.1 \times 10^{33} d_4^2 \text{ erg s}^{-1}$, could also be used to estimate \dot{E} from the L_X – \dot{E} corre-

⁷ A recently discovered PWN candidate in HESS J1632-408 (Balbo et al. 2010) also shows a steep spectrum with $\Gamma = 3.4_{-0.6}^{+0.6}$. However, the authors did not consider a possible contribution of a dust halo, which may be quite substantial given the very large $N_{\text{H}} \simeq 1.3 \times 10^{23} \text{ cm}^{-2}$ they measured in X-rays.

⁸ Tori radii in bright, well-resolved PWNe exceed r_s by a factor of 2 on average (Bamba et al. 2010).

lation (see Kargaltsev & Pavlov 2008, for recent results). Although this correlation shows a very large scatter, the plausible range for $\dot{E} \sim 10^{36} - 10^{37}$ erg s $^{-1}$ is in a good agreement with the above estimated value.

3.2. The nature of HESS J1834–087, 1FGL J1834.3–0842c, and CXOU J183434.9–084443

HESS J1834–087 belongs to the growing group of Galactic TeV sources that lack firm classifications or identifications with lower-energy counterparts. There are currently about 25 TeV sources in this group, of which only five can be considered truly “dark” sources (i.e., those without any detected counterparts) while the rest of the sources are coincident with one or more lower-energy sources of a known nature (SNRs, massive open stellar clusters, GMCs, X-ray binaries), which could, in principle, power the TeV emission (although there are no clear-cut cases). Spatial coincidence with W41 puts HESS J1834–087 in the latter category. As such a good positional match between a TeV source and a bright radio SNR is very unlikely to happen by chance, HESS J1834–087 must have physical relation to W41. This naturally leaves only two options for the origin of HESS J1834–087, a relic PWN or an SNR shock interacting with the GMC, both of which have been previously discussed (M+09, Tian et al. 2007).

Our detection of extended emission around CXOU J183434.9–084443 does not provide a convincing argument in favor of either of these two possible interpretations. Proving that CXOU J183434.9–084443 is a pulsar (e.g., by detecting pulsations) would provide a very strong support to the relic PWN hypothesis. Despite our highly significant detection of extended emission around CXOU J183434.9–084443, it is difficult to unequivocally establish its origin because of the very high absorption and a high likelihood of a significant dust scattering halo. It appears that a better way to go about establishing the nature of CXOU J183434.9–084443 would be a sensitive timing search in X-rays and GeV. However, even if CXOU J183434.9–084443 turns out to be a pulsar, there will remain a question about the origin of the nearby *Fermi* LAT source 1FGL J1834.3–0842c (see Figure 4), which is located within W41 but offset from both the center of the TeV source and from CXOU J183434.9–084443, and even more offset from the patch of the large-scale X-ray emission, which could be a relic PWN akin to the Vela X PWN (see above). Unless the 1FGL source is not real⁹ or its position is inaccurate, a separate interpretation would be required. While awaiting for better *Fermi* image, we can speculate that 1FGL J1834.3–0842c might be able to provide a long-sought evidence of hadrons in a pulsar wind (e.g., Arons 2009; Bednarek 2007). Indeed, the positional coincidence with the SNR suggests that the GeV emission can be produced by pulsar-wind protons interacting with the dense material of the part of the SNR shell, which intriguingly turns out to be the nearest to the putative pulsar. We must admit, however, that until the pulsar nature of CXOU J183434.9–084443 is firmly established the above reasoning will remain

highly speculative.

On the other hand, a failure to find pulsations from CXOU J183434.9–084443, down to a restrictive limit for a young pulsar, would strongly suggest that it is an unrelated source. In this case, one would be forced to conclude that there is no plausible candidate for a young pulsar within W41. This would imply that the TeV emission is most likely produced by the interaction of protons accelerated in the SNR shock with a particularly dense material in the nearby molecular cloud (Tian et al. 2007; Albert et al. 2006). Obtaining a firm evidence of this would be of a great interest because so far there are very few TeV sources (HESS J1745–303A, HESS J1800–240AB, HESS J1848–018) where the interaction with the nearby molecular cloud is considered as a possible (albeit not firmly established) mechanism of the VHE emission. Since HESS J1834–087 is located well within the W41 shell and has a significantly smaller diameter, it could only be associated with a part of the shell projected within the W41 interior on the sky. The offset between the TeV and 1FGL sources would be even more difficult to explain than in the PWN interpretation. Also, one would have to conclude that the large-scale X-ray emission (see Section 2.1.2) must be associated with the SNR interior, which would require rather high temperatures to explain the measured hard spectrum (M+09).

Keeping in mind the uncertainty in the interpretations, we opt to plot the multiwavelength PWN spectral energy distribution (Figure 7) but refrain from any modeling, which would be premature due to the large number of options afforded by the existing data. We note, however, that the GeV and TeV spectra generally seem to match, which hints at their common origin and a possible inaccuracy in the determination of the 1FGL J1834.3–0842c position. Alternatively, the observed GeV emission coinciding with the part of the shell could be produced by protons interacting with hadrons in the SNR shell and producing neutral pions that decay emitting the observed γ -rays. The relativistic protons may be accelerated either in the PW (e.g., Arons 2009; Bednarek 2007) or by the SNR shock interacting with the molecular clouds, which has been also previously proposed as the source of the TeV emission (Tian et al. 2007; Albert et al. 2006).

4. CONCLUSION AND SUMMARY

Our *Chandra* observation resolved the extended X-ray emission in the immediate vicinity of CXOU J183434.9–084443, by far the brightest X-ray source within the HESS J1834–087 extent. The source and the accompanying extended emission are strongly absorbed in X-rays leading to significant uncertainties in their spectra, which fit PL models with quite different slopes. The spectrum of the extended emission is markedly softer suggesting that the emission might be a dust scattering halo. Alternatively, the difference in the slopes could be due to the strong synchrotron cooling, if the extended emission is a PWN. Although our approximate dust scattering halo calculations allow us to obtain a reasonable fit to the observed radial profile of the extended emission, large uncertainties in the dust scattering model preclude us from definitive judgment on the nature of the extended emission, leaving a PWN option as a still viable alternative. The previously reported faint, large-scale extended emission appears to be disjoined from CXOU J183434.9–

⁹ It is marked as “confused” in the 1FGL catalog, which means that it might be the result of an imperfect model of the diffuse Galactic background (see Abdo et al. 2010, for details).

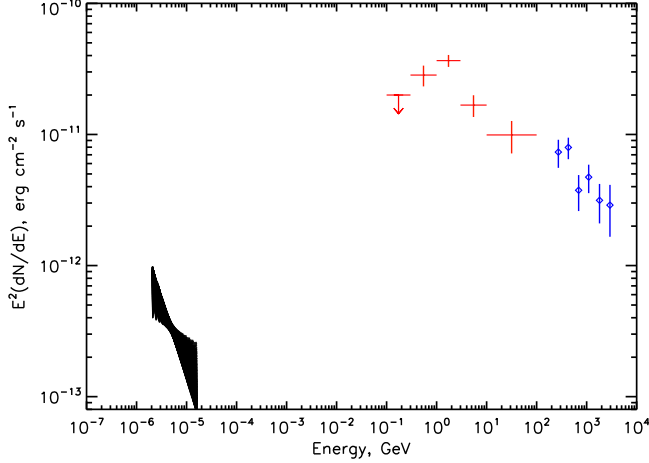


FIG. 7.— Broad-band spectrum of the PWN candidate showing the X-ray spectrum (ACIS, black) and the catalogued GeV (*Fermi*, red) and TeV (HESS, blue) emission. The TeV nebula spatially overlaps with the X-ray PWN candidate, while the GeV emission is located between the TeV nebula and part of the SNR shell (see Figure 4).

084443 in a better resolution *Chandra* image, which rules out a pulsar tail hypothesis and suggest that it might either be a part of a displaced relic PWN or a surprisingly hot plasma in the SNR interior.

Adjacent to the TeV source, and overlapping with a part of the SNR shell, there is extended GeV emission, the *Fermi* LAT source 1FGL J1834.3-0842c. The offset from HESS J1834-087 and CXOU J183434.9-084443

complicates the interpretation of the GeV emission suggesting that either the 1FGL J1834.3-0842c's position is inaccurate or it could be an intriguing case of a pulsar wind interacting with the SNR shell via hadronic mechanism. The X-ray timing and deeper imaging observations are required to understand the nature of CXOU J183434.9-084443 and of the offset large-scale X-ray emission. Together with improved GeV data, this will make it possible to identify HESS J1834-087 and 1FGL J1834.3-0842c, and determine the nature of their relationship with W41.

We also serendipitously observed the recently discovered SGR J1833-0832, which, however, was not detected. We place a limit of 3×10^{-14} ergs s $^{-1}$ cm $^{-2}$ on its unabsorbed flux, which is a factor of 40 dimmer than was measured by Göğüş et al. (2010).

Support for this work was provided by the National Aeronautics and Space Administration through *Chandra* Award Number GO9-0076X issued by the *Chandra* X-ray Observatory Center, which is operated by the Smithsonian Astrophysical Observatory for and on behalf of the National Aeronautics Space Administration under contract NAS8-03060. The work was also partially supported by NASA grants NNX09AC84G and NNX09AC81G, and NSF grants No. 0908733 and 0908611. G. G. P was partly supported by the Ministry of Education and Science of the Russian Federation (contract 11.634.31.0001).

APPENDIX

DUST HALO MODEL

Dust halos, often seen around bright point-like X-ray objects, are formed by scattering of source X-ray photons on dust grains. Here we will only discuss the case of dust optically thin with respect to the photon scattering, $\tau_{\text{scat}} \lesssim 1$, and consider only azimuthally symmetric halos (which implies that the dust distribution across the line of sight (LOS) is uniform within the interval of angles θ at which we see the halo). In this case the spectral halo intensity (ph cm $^{-2}$ s $^{-1}$ keV $^{-1}$ arcmin $^{-2}$) is given by the equation

$$I_{\text{halo}}(\theta, E) = F(E) N_H \int_0^1 dx \frac{f(x)}{x^2} \frac{d\sigma_s(E, \theta_s)}{d\Omega_s}, \quad (\text{A1})$$

where $F(E)$ is the point source spectral flux (photons cm $^{-2}$ s $^{-1}$ keV $^{-1}$), $x = (D - d)/D$ is the dimensionless distance from the X-ray source to the scatterer (D and d are the distances from the observer to the source and the scatterer, respectively), $\theta_s \simeq \theta/x$ (for small angles) is the scattering angle, $f(x)$ is the dimensionless dust density distribution along the LOS ($\int_0^1 f(x) dx = 1$), and $d\sigma_s(E, \theta_s)/d\Omega_s$ is the differential scattering cross section per one hydrogen atom, averaged over the dust grain distribution over sizes and other grain properties (see, e.g., Mathis & Lee 1991).

To understand the halo properties from simple analytical expressions, we will use the Rayleigh-Gans (RG) approximation, in which the total scattering cross section $\propto E^{-2}$; this approximation works better for higher energies, $E \gtrsim 0.5$ –2 keV, depending on the dust model. For some dust models, the averaged differential cross section in the RG can be approximated as (Draine 2003)

$$\frac{d\sigma_s(E, \theta_s)}{d\Omega_s} \approx \frac{\sigma_s(E)}{\pi \theta_{s,50}^2} \frac{1}{(1 + \theta_s^2/\theta_{s,50}^2)^2}, \quad (\text{A2})$$

where

$$\theta_{s,50} \approx \frac{\Theta}{E} \quad \text{and} \quad \sigma_s(E) \approx \frac{S}{E^2} 10^{-22} \text{ cm}^2 \quad (\text{A3})$$

are the median scattering angle and the total cross section, respectively; E is the energy in keV. The constant Θ in first eq. (A3) depends on the dust model; Draine (2003) derived $\Theta = 360''$ from the dust model of Weingartner & Draine (2001), while Bocchino et al. (2010) found $\Theta = 7.4'$ for the model of Smith & Dwek (1998).

It follows from the second eq. (A3) that the scattering optical depth is

$$\tau_{\text{scat}}(E) \approx SN_{H,22}E^{-2}. \quad (\text{A4})$$

The factor S in the second eq. (A3) is a constant of the order of 1; e.g., $S \approx 1.3$ from Figure 6 of Draine (2003), while Predehl & Schmitt (1995) found a mean value $S \approx 0.49$ for a number of halos observed with *ROSAT* (but the scatter was very large), while Mathis & Lee (1991) discuss models with $S = 0.903, 1.09$, and 0.47 (see their Table 1). Costantini (2004; PhD thesis) estimated $\tau_{\text{sca}}(1 \text{ keV})$ for a number of halo sources observed with *Chandra*; the values of S derived from her results show a very strong scatter, S from 0.018 to 2.26. The scatter itself may be natural, as the dust properties may be different for different sources.

It should be noted that the correlation of $\tau_{\text{sca}}(1 \text{ keV})$ with visual extinction A_V :

$$\tau_{\text{scat}}(1 \text{ keV}) = (0.056 \pm 0.01)A_V \quad (\text{A5})$$

(Predehl & Schmitt 1995) is better than that with N_H , but A_V is rarely known for the objects of interest.

Substituting (A2) and (A3) in (A1), we obtain the spectral intensity profile

$$I_{\text{halo}}(\theta, E) = F(E)N_{H,22}\frac{S}{\pi\Theta^2} \int_0^1 \frac{f(x)}{x^2} \left[1 + \left(\frac{\theta E}{x\Theta} \right)^2 \right]^{-2} dx. \quad (\text{A6})$$

For comparison with the point source + halo profile observed in the energy range $E_1 < E < E_2$, the sum of the spectral intensities should be convolved with the detector response, with allowance for the image spread caused by the telescope and the detector. We have checked that the energy redistribution in the detector only slightly affects the broadband radial profile for a smooth incident spectrum. Therefore, assuming the observable halo size to be much larger than the PSF width, we obtain

$$I_{\text{obs}}(\theta) = \int_{E_1}^{E_2} dE A_{\text{eff}}(E) F(E) \left\{ \psi(\theta, E) + N_{H,22} \frac{S}{\pi\Theta^2} \int_0^1 dx \frac{f(x)}{x^2} \left[1 + \left(\frac{\theta E}{x\Theta} \right)^2 \right]^{-2} \right\}, \quad (\text{A7})$$

where $A_{\text{eff}}(E)$ is the detector's effective area, and $\psi(\theta, E)$ is the normalized PSF, which can be taken from a simulation (e.g., with MARX). The first term in Equation (A7) corresponds to the point source, while the second term describes the halo.

The above equation can be integrated for a given set of halo parameters, and compared directly with the data. In particular, for the dust halo model shown in Figure 3 we picked $\Theta = 360''$, $S = 1$, and the dust distribution function

$$f(x) = \begin{cases} x_o^{-1}, & x \leq x_o \\ 0, & x > x_o \end{cases} \quad (\text{A8})$$

with $x_o = 0.25$. According to (A6), this distribution function corresponds to

$$\begin{aligned} I_{\text{halo}}(\theta, E) &= \frac{F(E)N_{H,22}Sa}{2\pi(x_o\Theta)^2} \left(\arctan a - \frac{a}{1+a^2} \right) \\ &\approx \frac{F(E)N_{H,22}Sa}{4x_o^2\Theta^2} \begin{cases} 1 & a \gg 1 \\ (3\pi)^{-1}a^3 & a \ll 1 \end{cases} \end{aligned} \quad (\text{A9})$$

where $a = x_o\Theta/\theta E$.

REFERENCES

- Abdo, A. A., et al. 2010, *ApJS*, 188, 405
 Acero, F., Ballet, J., Decourchelle, A., Lemoine-Goumard, M., Ortega, M., Giacani, E., Dubner, G., & Cassam-Chenai, G. 2009, *A&A*, 505, 157
 Aharonian, F., et al. 2005, *Science*, 307, 1938
 Aharonian, F., et al. 2006, *ApJ*, 636, 777
 Albert, J., et al. 2006, *ApJ*, 643, L53
 Arons, J. 2009, in *Astrophysics and Space Science Library*, Vol. 357, *Astrophysics and Space Science Library*, ed. W. Becker, 373
 Balbo, M., Saouter, P., Walter, R., Pavan, L., Tramacere, A., Pohl, M., & Zurita-Heras, J. 2010, *A&A*, 520, A111
 Bamba, A., Mori, K., & Shibata, S. 2010, *ApJ*, 709, 507
 Bartko, H., & Bednarek, W. 2008, *MNRAS*, 385, 1105
 Bednarek, W. 2007, *Ap&SS*, 309, 179
 Bocchino, F., Bandiera, R., & Gelfand, J. 2010, *A&A*, 520, A71
 de Jager, O. C., & Djannati-Ataï, A. 2008, *ArXiv* 0803.0116
 Dickey, J. M., & Lockman, F. J. 1990, *ARA&A*, 28, 215
 Draine, B. T. 2003, *ApJ*, 598, 1026
 Gaensler, B. M., & Johnston, S. 1995, *MNRAS*, 275, L73
 Gallant, Y. A., et al. 2008, in *American Institute of Physics Conference Series*, Vol. 983, 40 Years of Pulsars: Millisecond Pulsars, Magnetars and More, ed. C. Bassa, Z. Wang, A. Cumming, & V. M. Kaspi, 195
 Gelbord, J. M., et al. 2010, *GRB Coordinates Network*, Circular Service, 10526, 1, 526, 1
 Gelbord, J. M., & Vetere, L. 2010, *GRB Coordinates Network*, Circular Service, 10531, 1, 531, 1
 Göğüş, E., et al. 2010, *ApJ*, 718, 331
 Hinton, J. A., & Hofmann, W. 2009, *ARA&A*, 47, 523
 Kargaltsev, O., Misanovic, Z., Pavlov, G. G., Wong, J. A., & Garmire, G. P. 2008, *ApJ*, 684, 542
 Kargaltsev, O., & Pavlov, G. G. 2008, in *American Institute of Physics Conference Series*, Vol. 983, 40 Years of Pulsars: Millisecond Pulsars, Magnetars and More, ed. C. Bassa, Z. Wang, A. Cumming, & V. M. Kaspi, 171

- Kargaltsev, O., & Pavlov, G. G. 2010, in American Institute of Physics Conference Series, Vol. 1248, American Institute of Physics Conference Series, ed. A. Comastri, L. Angelini, & M. Cappi, 25
- Kassim, N. E. 1992, *AJ*, 103, 943
- LaMassa, S. M., Slane, P. O., & de Jager, O. C. 2008, *ApJ*, 689, L121
- Landi, R., et al. 2006, *ApJ*, 651, 190
- Mathis, J. S., & Lee, C. 1991, *ApJ*, 376, 490
- Mukherjee, R., Gotthelf, E. V., & Halpern, J. P. 2009, *ApJ*, 691, 1707 (M+09)
- O’C. Drury, L., Aharonian, F. A., Malyshev, D., & Gabici, S. 2009, *A&A*, 496, 1
- Predehl, P., & Schmitt, J. H. M. M. 1995, *A&A*, 293, 889
- Smith, R. K., & Dwek, E. 1998, *ApJ*, 503, 831
- Tian, W. W., Li, Z., Leahy, D. A., & Wang, Q. D. 2007, *ApJ*, 657, L25
- Walter, R., et al. 2006, *A&A*, 453, 133
- Weingartner, J. C., & Draine, B. T. 2001, *ApJ*, 548, 296
- Yamazaki, R., Kohri, K., Bamba, A., Yoshida, T., Tsuribe, T., & Takahara, F. 2006, *MNRAS*, 371, 1975